ECCM18 - 18th European Conference on Composite Materials
Athens, Greece, 24-28th June 2018

Interlaminar shear strength enhancement under out-of-plane compression of fabric reinforcements - a review on meso and macro scale

Christian Düreth[1], **Daniel Weck**[1], **Robert Böhm**[1], **Mike Thieme**[1], **Maik Gude**[1]
[1] *Technische Universität Dresden, Institute of Lightweight Engineering and Polymer Technology, Holbeinstraße 3, 01307 Dresden, Germany*
E-mail: christian.duereth@tu-dresden.de

Carl H. Wolf[2], **Sebastian Henkel**[2], **Horst Biermann**[2]
[2] *Technische Universität Bergakademie Freiberg, Institute of Materials Engineering, Gustav-Zeuner-Straße 5, 09599 Freiberg, Germany*

Keywords: interlaminar shear, out-of-plane properties, RVE modelling, finite element analysis

Abstract

The shear strength enhancement under moderate out-of-plane respectively through-thickness compression is experimentally affirmed in biaxial testings (τ_{31}/σ_3^--testing). This phenomenological evidence can reliably be described either by maximum strain failure criteria or by an invariant based failure criterion. Nevertheless their scale is macroscopic and they all neglect the influence of the fabric architecture and stress interactions on the failure behaviour. Thus a representative volume element (RVE) analysis on meso scale of three different plain weave fabrics has been conducted to investigate the influence of higher ondulation and nesting on the failure occurrence.

1 Introduction

Fabric reinforcements gain an increasing usage in modern advanced composite structures, because of their inherent advantages [1]. Generic applications are fan blades, profiled drive shafts and bolted joints, which are characterised by superimposed stress states, like in-plane tensile or out-of-plane shear stresses combined with through-thickness compressive stresses (σ_1/σ_3^-- and τ_{31}/σ_3^-- stress states) [2, 3]. Especially interlaminar shear stresses (τ_{31}) are to be regarded as failure-critical for fabric reinforced carbon fibre thermosets.
In biaxial testing it has been experimentally proven that through-thickness compression enhances the interlaminar shear strength[1]. Many failure criteria proposed in literature can describe this phenomenological and empirical evidence either by a maximum failure strain criterion, such as Daniels [4], Sun [5] or Christensen et al. [6], or by an invariant based failure criterion, such as Cuntze [7]. Nevertheless these criteria are on a macroscopic level and neglect the influence of the fabric architecture. In order to assess these phenomena, three types of plain weave fabric, with different areal weight, have been chosen for experimental and numerical investigations. By increased areal weight the ondulation increases, thus the interlocking of adjacent fabric layers (nesting) is promoted and different stress states between the layers may occur.
To obtain these stress interactions and the failure levels according to a physically based failure criterion (Cuntze), a finite element analysis (FEA) with representative volume elements (RVE) and the embedded elements method (EEM) have been conducted [8, 9, 10]. The nominal weave

[1] will be published on the European Solid Mechanics Conference 2.-6. July 2018 in Bologna ("Experimental and numerical characterisation of the fracture behaviour of novel specimens for superimposed out-of-plane stresses")

architecture/geometry for maximum nesting and no nesting configuration had been obtained by the analysis of compressed dry layers through computer tomography [11]. Furthermore the displacements for the periodic boundary conditions (BC) have been extracted from a macroscopic FE-model, that has been verified by the experimental results.

2 Experimental

The experimental studies were conducted on a servo hydraulic planar biaxial testing system INSTRON 8800 (cf. figure 1a). This system incorporates four orthogonally aligned actuators, which can provide a load of up to 250 kN. Additionally, a stereo camera system, ARAMIS® 5M, for image acquisition was pointed at the region of interest. In a post-scripting process these images have been assessed by a digital image correlation software, ARAMIS® 2017, to determine the displacements and hence the strains of the τ_{31}/σ_3^--specimens' surface.

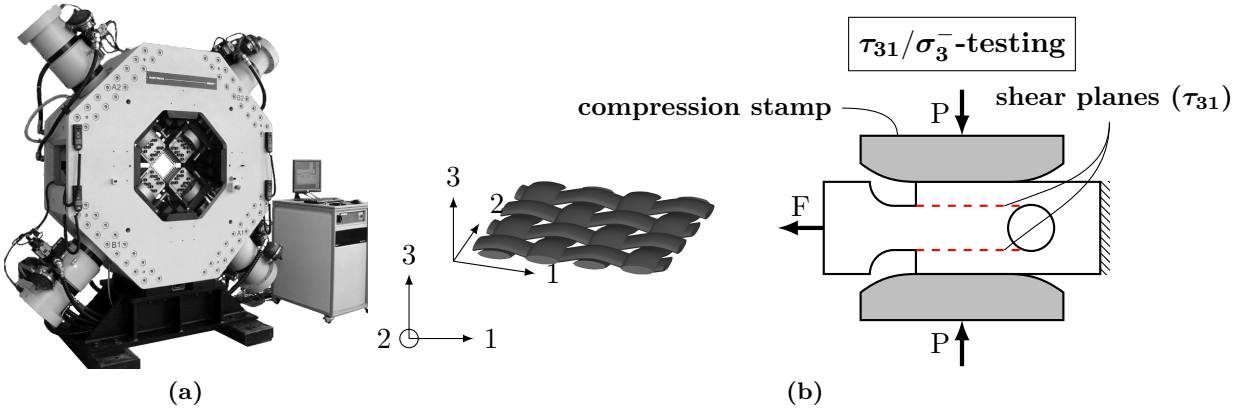

Figure 1: (a) Servo hydraulic planar biaxial testing system INSTRON 8800; (b) fabric plain weave pattern and its corresponding material coordinate system (left), schematic illustration of the τ_{31}/σ_3^--specimen and its boundary conditions (right)

This specimen design has been numerically and experimentally developed to achieve an homogeneous shear stress distribution in the shear areas [2]. To avoid premature failure, radii have been added at the notches' outer corners. Furthermore, the stamp design was iteratively developed to decrease the HERTZIAN contact pressure by adding preferable big radii at the stamps' boundaries of its contact surface (cf. figure 1b).

Table 1: Selected properties of the plain weave fabric types

fabric type	I	II	III
roving	TENAX-E® HTMA 3K		
ECC-style	447	450	470
weave	plain weave		
areal weight [g/m^2]	160	200	285
setting [threads/cm]	4	5	7

Three different types of plain weave fabric (cf. table 1) have been used to compound the τ_{31}/σ_3^--specimen with the aerospace thermoset RTM6 in a resin transfer moulding process. Three different plates with an estimated fibre volume fraction of 60 %, a density of 1.52 g/cm^3 and a thickness of 10 mm have been processed. After cutting the specimens to a width of 10 mm, the hole notch pattern has been added by milling and drilling.

In the quasi-static biaxial experiments different load paths (τ_{31}/σ_3^--ratios: 1:0, 1:1 and 1:2) were applied with a force rate of 2 kN/s to determine the effect of through-thickness compression on the interlaminar shear strength.

3 Numerical

The macroscopic model conduces for the derivation of the displacements for the quasi-periodic BCs of the RVE. For a reliable approximation the results of the numerical computation were compared with the strain-field measurement obtained by ARAMIS® (cf. figure 2).

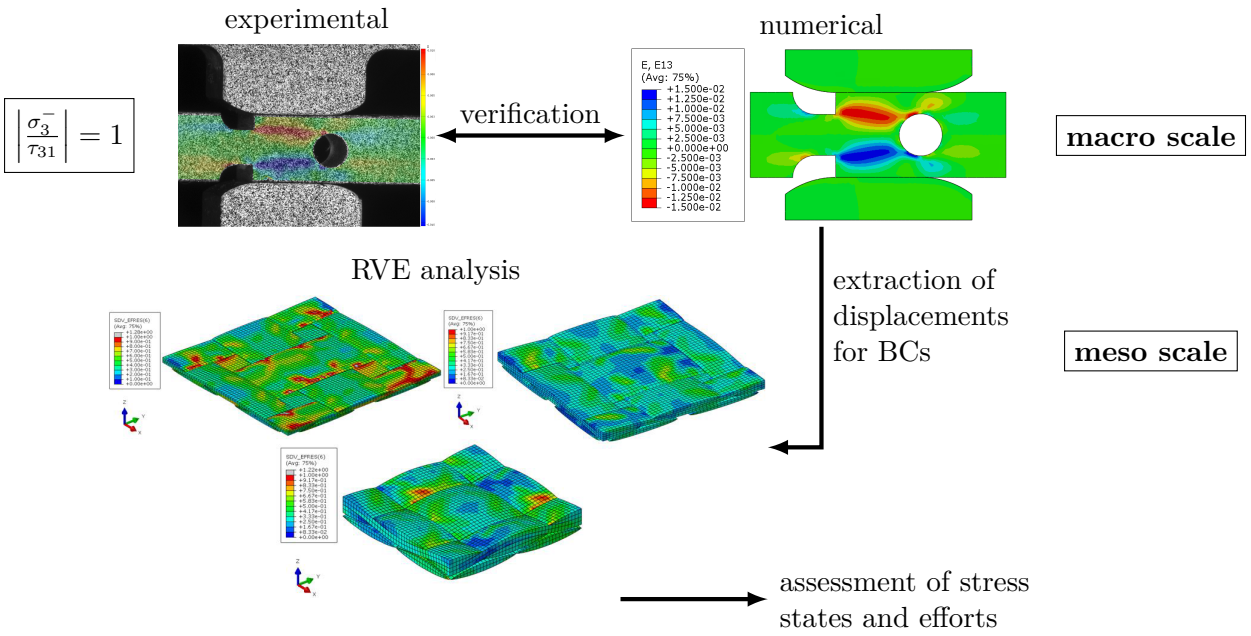

Figure 2: Schematic work flow of the finite element analysis (FEA) on macro and meso scale

The RVE analysis was conducted in Abaqus®. For each fabric type a maximum nesting and a no nesting configuration have been modelled by the embedded elements method. The following sections will explicitly explain the macro- and mesoscopic models.

3.1 Macroscopic FEA

In reference to the nominal τ_{31}/σ_3^--specimen geometry, evaluated in [2], the model has been created in the area of the hole notch pattern and meshed with C3D8R-elements (cf. figure 2). Additionally, the contact behaviour between the stamps and the specimen has been defined by a '*hard contact*' in normal direction and by a Coulomb friction model ($\mu = 0.15$ [12]) in tangential direction [13].
In the model a linear elastic material behaviour has been used for the orthotropic composite material of the specimen and the isotropic stamp material (Marage 300; $E = 193$ GPa, $\nu = 0.34$). Table 2 lists the material data, which were determined by uniaxial standard testings for each fabric type.
The values for the NEUMANN BC, according to figure 1b, were derivated from the pre-failure step of the acquired images by the stereo-camera system to achieve an accurate copy. Hence it was feasible to compare the values of γ_{13} along both shear plane paths, cf. figure 1b, in a post-scripting process to determine the goodness of the numerical assumption. After verification, the displacements for the RVEs' BCs were derivated from the macroscopic model taking into account the RVE dimensions of the considered fabric types.

Table 2: Elastic material properties of the selected fabric reinforced thermosets - determined by standard test methods and used in macroscale simulation

fabric type	E_1 [GPa]	$E_2{}^*$ [GPa]	E_3 [GPa]	G_{12} [GPa]	G_{13} [GPa]	$G_{23}{}^*$ [GPa]	ν_{12} [−]	ν_{13} [−]	$\nu_{23}{}^*$ [−]
I	73.20	73.20	10.90	5.22	3.15	3.15	0.123	0.013	0.013
II	69.40	69.40	11.50	4.95	3.40	3.40	0.080	0.015	0.015
III	66.10	66.10	10.80	5.00	3.16	3.16	0.134	0.015	0.015

* symmetrical assumption

3.2 Mesoscopic FEA

In experimental studies of the compressed dry fabric, the nominal weave geometry has been obtained for each fabric type by computer tomography [11]. The re-creation of a three-dimensional model of each weave pattern was performed in TexGen®. Thereby two configurations, maximum nesting and no nesting, for each fabric type are preferably to be considered, to identify the influence of the composite structure on the mesoscalic stress states and resulting apparent interlaminar shear strength.
The meshing was ensued in Abaqus® by the EEM. This method is a mesh superposition based concept to obtain a good quality mesh for matrix and roving. Thereby the matrix (host part) and reinforcement (embedded part) are meshed separately, but are related by their translational degrees of freedom [9, 10].

Table 3: Analytically estimated elastic material properties for the roving and measured values for isotropic matrix behaviour (used in mesoscale simulation) [14]

	$E_\parallel$ [GPa]	$E_\perp$ [GPa]	$G_{\parallel\perp}$ [GPa]	$G_{\perp\perp}$ [GPa]	$\nu_{\parallel\perp}$ [−]	$\nu_{\perp\perp}$ [−]
Roving*	172.229	18.548	9.280	6.941	0.272	0.336
	E [GPa]	ν [−]				
Matrix	3.354	0.38				

*FVC of 72 %

The elastic properties of the roving, approximated as an unidirectional composite, were evaluated by a semi-empirical analytical solution presented in [14] (cf. table 3). The fibre volume content (FVC) of 72 % was experimentally determined by a microscopical image analysis, which includes a *Hough Circle Transformation* and a *Delaunay Triangulation* to compute the local FVC, from different rovings' cross sections. The elastic properties for the isotropic matrix were experimentally determined in [15].
For an unidirectional composite, five failure modes according to Cuntze are considerable [7]. Hence the resultant stress effort can be derivated to

$$EFF^{(res)^{\dot{m}}} = \left(\frac{\sigma_{eq}^{\parallel\sigma}}{R_\parallel^+}\right)^{\dot{m}} + \left(\frac{\sigma_{eq}^{\parallel\tau}}{R_\parallel^-}\right)^{\dot{m}} + \left(\frac{\sigma_{eq}^{\perp\sigma}}{R_\perp^+}\right)^{\dot{m}} + \left(\frac{\sigma_{eq}^{\perp\tau}}{R_\perp^-}\right)^{\dot{m}} + \left(\frac{\sigma_{eq}^{\perp\parallel}}{R_{\perp\parallel}}\right)^{\dot{m}}, \tag{1}$$

where $\parallel$ is the fibre parallel direction, $\perp$ is the transverse direction, $+$ indicates tensile and $-$ compression stresses respectively strengths (cf. table 4). The coefficient $\dot{m}$ has been set in the range of 2.5 to 4 according to [7]. Equation 1 was incorporated in a post-scripting subroutine in

Table 4: Semi-analytical and estimated strength properties of an unidirectional layer

$R_{\parallel}^{+}$ [MPa]	$R_{\parallel}^{-}$ [MPa]	$R_{\perp}^{+}$ [MPa]	$R_{\perp}^{-}$ [MPa]	$R_{\perp\parallel}$ [MPa]
2602	1152	70	211	98

*FVC of 72 %

Abaqus® to obtain the failure levels for each roving. Additionally, for the matrix rich zones an isotropic failure criterion for brittle material, like Tresca, has to be considered to asses failure in the interface zone.

4 Results and discussion

To briefly summarise the experimental results, through thickness compression (σ_3^-) enhances the interlaminar shear strength (R_{31}), as figure 3 illustrates. However, the corresponding failure stresses of each fabric type cannot be significantly distinguished to observe the influence of ondulation and fabric architecture, respectively.

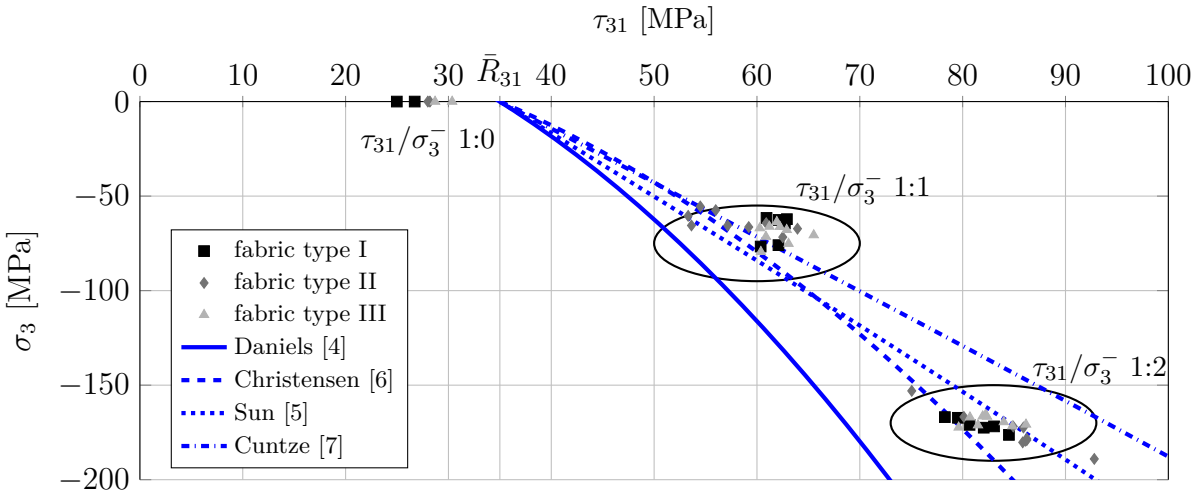

Figure 3: Results of biaxial testing and illustration of failure criteria of different authors

Supplementary, failure criteria of different authors are illustrated in figure 3. Average values from uniaxial standard tests of each fabric type were selected to describe the failure envelopes ($\bar{R}_{31}$, $\bar{G}_{13}$, etc.). A reliable convergence can be observed by the criteria of Sun and Christensen. On the contrary, Cuntze and Daniels expose a divergent behaviour at load paths exceeding a ratio of $\tau_{31}/\sigma_3^- = 1{:}1$ respectively even lower.
The macroscopic FEA result showed a reliable convergence to the extracted strain field from Aramis® as figure 4 illustrates. The comparison was obtained for the ratio of 1:1 (τ_{31}/σ_3^-) for fabric type II and the γ_{31}-strains were extracted at the shear planes (cf. figure 1b). Thereby a *root mean square error*[2] (RMSE) of 0.0051 for cut 1 respectively 0.0081 for cut 2 could be determined. Hence it is feasible to extract the displacements for the RVE analysis from the macroscopic FE model.

[2] $RMSE = \sqrt{\frac{\sum_{i=1}^{n}(\hat{y}_i - y_i)^2}{n}}$, where $\hat{y}_i$ are predicted values, y_i are measured values and n is the count of discrete data points

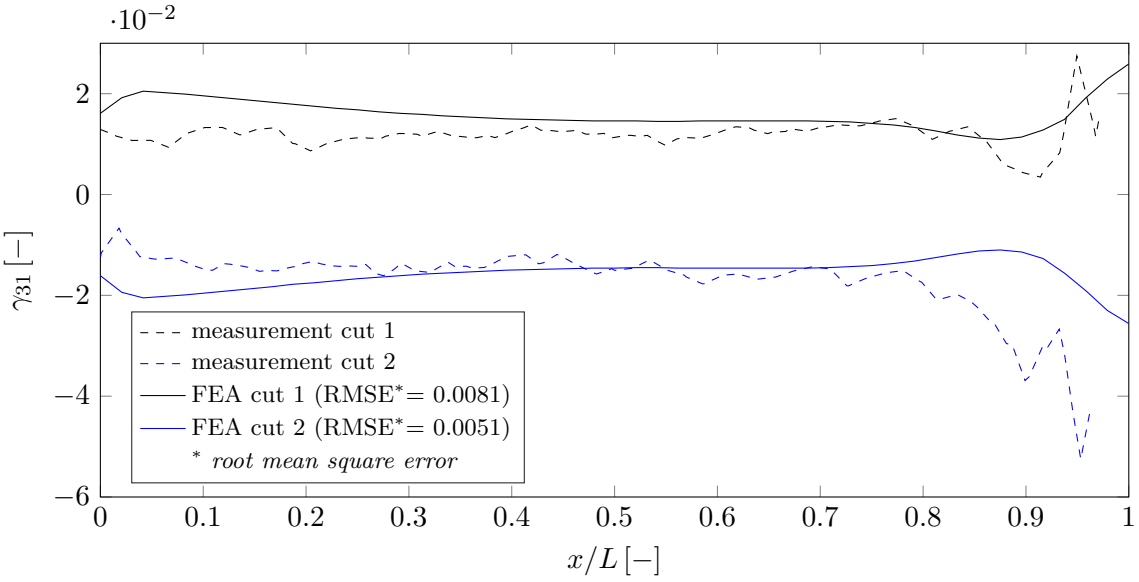

Figure 4: Comparison of FEA results and determined strain field by ARAMIS® in the shear areas (load ratio $\tau_{31}/\sigma_3^- = 1{:}1$, fabric type II)

Results of the analysis of the RVE models for load ratio τ_{31}/σ_3^- 1:2 are shown in figure 5. Overall, the efforts of critical failure modes (e.g. fibre parallel tension and compression) do not reach the failure limit $EFF = 1$. Hence, total failure of the roving composite is not expected. Nevertheless, the resulting stress efforts $EFF^{(res)}$ by CUNTZE exceed the limit of 1 which indicates first damages in the composite of the rovings due to the present stress state. Also, the resulting stress efforts $EFF^{(res)}$ show significant differences for the considered fabric configurations (cf. figure 5). For fabric type I and II, higher stress efforts occur in the no nesting configuration (figure 5(b) and (d)). These are induced in particular by local tensile stresses σ_3 at the edges of the transverse rovings, which result from a deformation of the longitudinal rovings. For fabric type II, high resultant stress efforts occur additionally in the longitudinal rovings, which are caused by a local tensile stress in the direction of the fibres due to the tilting of the transverse rovings. In comparison, fabric type III shows a more homogeneous stress effort distribution especially for the no nesting configuration. For the maximum nesting configuration of this fabric type, local maxima in the resultant stress effort at the edges of the transverse rovings evolve. These are likely to be caused by the deformation of the longitudinal rovings, which induce tensile stresses σ_3 and compressive stresses σ_2, respectively, in different areas of the transverse rovings. Provided that real laminates are always a mixture of no nesting and maximum nesting configurations, it can be concluded for load ratio τ_{31}/σ_3^- 1:2 that the highest strength is expected for fabric type III. This can be explained especially by local support effects due to the increased fibre ondulation.
Looking at the polymer matrix and the present equivalent stresses according to TRESCA, it can be determined that the distribution in the interface between the layers is significantly more inhomogeneous for no nesting configurations compared to maximum nesting configurations. Here, maxima of up to 96 MPa occur. For the maximum nesting configurations, the TRESCA stress distributions are more homogeneous, but the compressive stresses σ_3 are lower (cf. figure 6). This circumstance reduces the maximum bearable shear stresses τ_{13} according to MOHR-COULOMB and can thus promote an interlaminar shear failure. However, the mechanical clamping between the rovings in the maximum nesting configuration counteract this mode of failure.

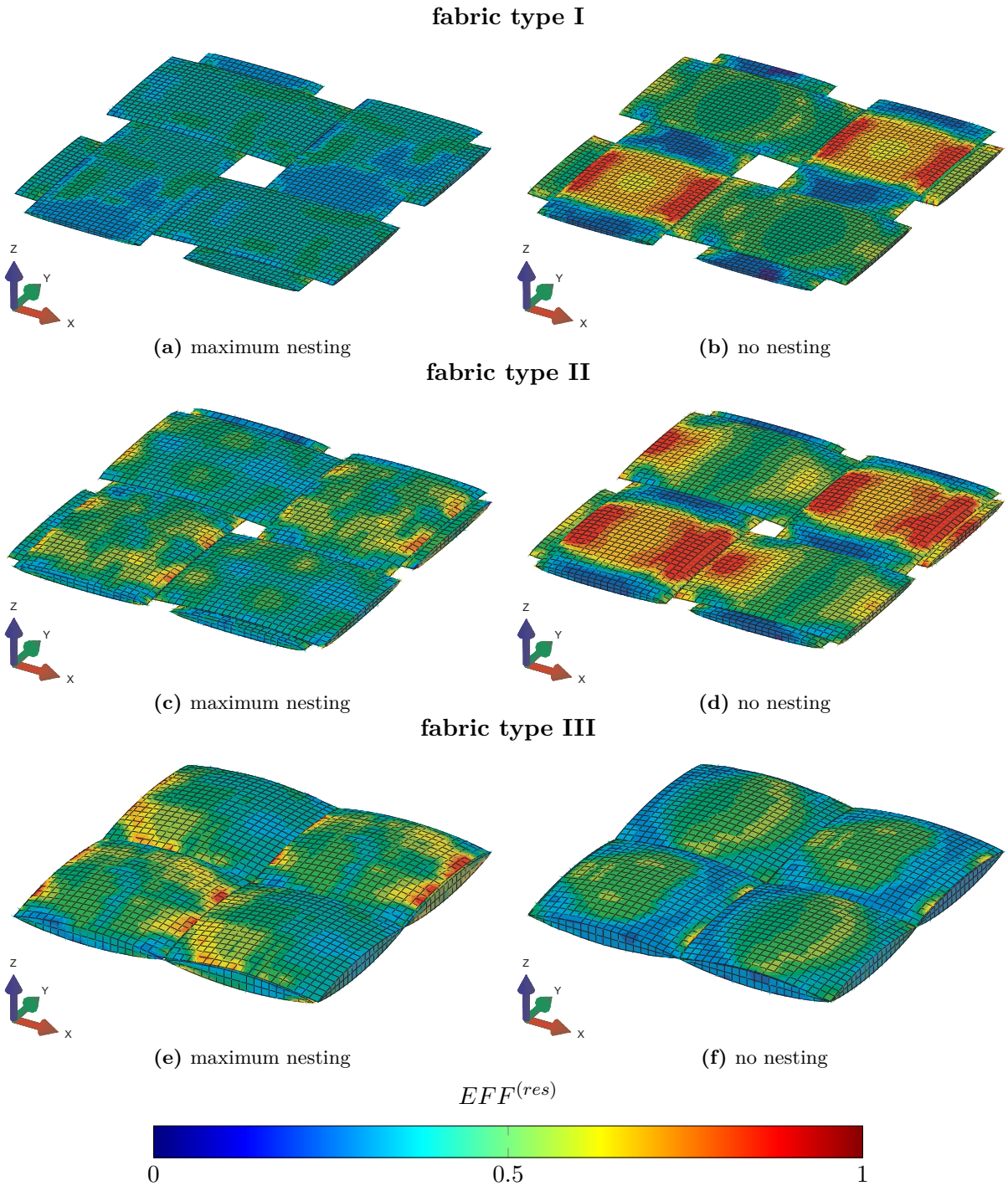

(a) maximum nesting **(b)** no nesting

(c) maximum nesting **(d)** no nesting

(e) maximum nesting **(f)** no nesting

Figure 5: Resultant stress effort $EFF^{(res)}$ by CUNTZE in the rovings of the analysed RVE (x-direction is equivalent to 1-axis, z-direction is equivalent to 3-axis of figure 1)

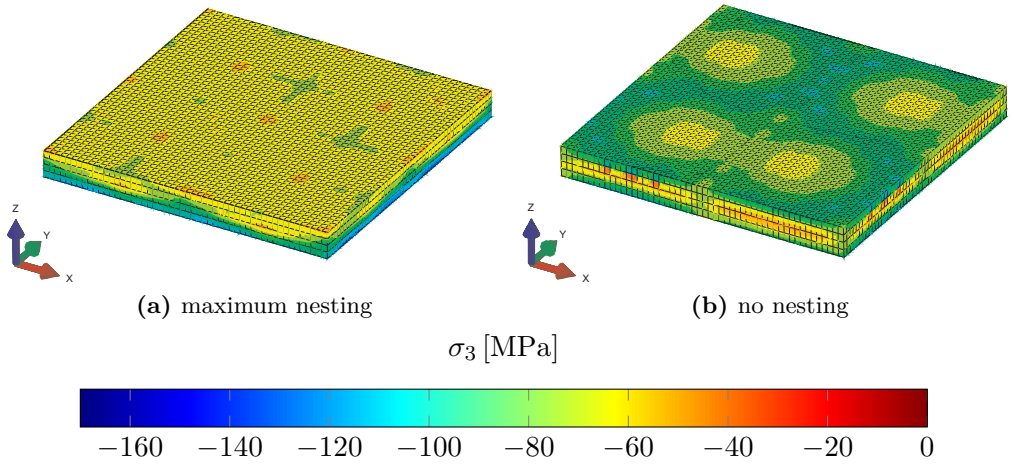

(a) maximum nesting **(b)** no nesting

Figure 6: Compressive stress σ_{33} within the polymer matrix at the interface of adjacent layers for fabric type III

5 Conclusion

The well-known interactions of failure modes within composite materials lead to altered load-bearing capacities under biaxial loading conditions. Within this study, a biaxial stress state of through-thickness compression and interlaminar shear was investigated. The presented results confirm that through-thickness compression enhances the interlaminar shear strength and plenty failure criteria, such as Sun and Christensen, can reliably describe this phenomenological evidence of the investigated materials. Nevertheless, in the range of intermediate through-thickness compression a difference in the total failure strengths of different fabric types could not be observed. Thus, an influence of the textile architecture cannot be ascertained on the macroscopic scale for that load range.
In order to examine the phenomena on the meso scale, FEA of the composite RVE were conducted. The BCs needed for these investigations were determined by means of a macroscopic FEA of the real test configuration. The feasibility of the presented work flow to determine the BCs for the RVE FEA is confirmed by a reliable approximation of the strain field measured by Aramis® during the biaxial material tests.
In the mesoscopic FE analyses the influence of the plain weave fabric architecture could be determined. On the one side it was observed that for fabric types I and II (lower areal weight) the no nesting configurations show significantly increased resultant stress efforts by Cuntze in the longitudinal rovings in comparison to the maximum nesting configuration. On the other side a lower resultant stress effort $EFF^{(res)}$ was determined for fabric type III (highest areal weight) for both nesting configurations. Furthermore it was observed that especially the maximum nesting configuration decreases the compressive stress (σ_3) in certain specific areas, thus the apparent interlaminar shear strength decreases according to Mohr-Coulomb-criterion for isotropic brittle material.
However, it could be phenomenologically observed that the fracture pattern occurs between two layers. Hence the matrix rich interface zone should be further investigated in subsequent studies to assess the influence of the fabric architecture and corresponding failure stresses.

Acknowledgement

The authors gratefully acknowledge the financial support of the German Research Foundation (DFG - GU 614/8-1).

References

[1] B. Harris. *Fatigue in composites: Science and technology of the fatigue response of fibre-reinforced plastics*. Cambridge: Woodhead Publishing Limited, 2000.

[2] H. Böhm, R. Schirner, and M. Gude. "Experimental and numerical investigation of appropriate CFRP specimen designs for inducing in-plane tensile/through-thickness compressive and interlaminar shear/through-thickness compressive stress states". In: *Proceedings of 8th International Conference on Composite Testing and Model Identification*. Leuven: KU Leuven, 2017.

[3] K. W. Gan, S. R. Hallett, and M. R. Wisnom. "Measurement and modelling of interlaminar shear strength enhancement under moderate through-thickness compression". In: *Composites* Part A.49 (2013), pp. 18–25.

[4] I. M. Daniel et al. "Interfiber/interlaminar failure of composites under multi-axial states of stress". In: *Composite Science and Technology* 69 (2009), pp. 764–771.

[5] C. Sun. "Strength analysis of unidirectional composites and laminates". In: *Comprehensive composite materials* (2000), pp. 641–666.

[6] R. M. Christensen and S. DeTeresa. "Delamination failure investigation for out-of-plane loading in laminates". In: *Composite Materials* 38.24 (2004), pp. 2231–2238.

[7] R. Cuntze and A. Freund. "The predictive capability of failure mode concept-based strength criteria for multidirectional laminates". en. In: *Composites Science and Technology* 64.3-4 (Mar. 2004), pp. 343–377.

[8] N. De Carvalho, S. Pinho, and P. Robinson. "Numerical modelling of woven composites: Biaxial loading". In: *Composites Part A: Applied Science and Manufacturing* 43.8 (2012), pp. 1326–1337.

[9] S. Tabatabaei and S. V. Lomov. "Eliminating the volume redundancy of embedded elements and yarn interpenetrations in meso-finite element modelling of textile composites". In: *Computers & Structures* 152 (2015), pp. 142–154.

[10] S. Tabatabaei and S. V. Lomov. "Embeeded Element Method in meso finite element modelling of textile composite". In: *Proceedings of 20th International Conference on Composite Materials*. Copenhagen, 2015, p. 12.

[11] R. Schirner, M. Süß, and M. Gude. "In-situ computed tomography of the compaction behaviour of single-ply and multi-ply carbon fibre woven fabrics". In: *The 10th Asian-Australasian Conference on Composite Materials (ACCM-10)*. Bexco in Busan, Korea, 2016.

[12] M. Andrich et al. "Characterisation of the friction and wear behavior of textile reinforced polymer composites in contact with diamond-like carbon layers". In: *Tribology International* 62 (2013), pp. 29–36.

[13] Dassault Systems. *Abaqus 6.14 Analysis User's Guide*. 2014.

[14] H. Schürmann. *Konstruieren mit Faser-Kunststoff-Verbunden*. Berlin Heidelberg: Springer, 2005.

[15] M. Andrich. "Analyse des Schädigungs- und Versagensverhaltens dickwandiger textilverstärkter Kunststoffverbunde bei Druckbelastung in Dickenrichtung". Dissertation. Technical University Dresden, 2013.